

# Keck Spectroscopy of Globular Clusters in the Sombrero Galaxy <sup>1</sup>

Søren S. Larsen and Jean P. Brodie

*UC Observatories / Lick Observatory, University of California, Santa Cruz, CA 95064, USA*

soeren@ucolick.org and brodie@ucolick.org

and

Michael A. Beasley and Duncan A. Forbes

*Astrophysics & Supercomputing, Swinburne University, Hawthorn VIC 3122, Australia*

mbeasley@mania.physics.swin.edu.au and dforbes@astro.swin.edu.au

## ABSTRACT

We analyze high signal-to-noise spectra for 14 globular clusters (GCs) in the Sombrero galaxy, NGC 4594 = M104, obtained with the LRIS spectrograph on the Keck I telescope. We find generally good agreement between spectroscopic metallicities and previous photometric metallicities based on  $V-I$  colors. Further, we use measurements of various Balmer line indices on co-added spectra of metal-poor and metal-rich GCs to estimate ages for the GC subpopulations and find ages of 10–15 Gyr, with preferred ages around 11–12 Gyr and no detectable differences between the metal-rich and metal-poor subpopulations. However, because of model and measurement uncertainties, age differences of a few (2–3) Gyrs cannot be ruled out. We also measure alpha to iron abundance ratios from Mg and TiO features and find enhancements on the order of  $[\alpha/\text{Fe}] \sim +0.4$ , similar to the  $[\alpha/\text{Fe}]$  abundance ratios observed in other old stellar populations. Finally, we combine our sample with radial velocities for 34 GCs from Bridges et al. (1997) and obtain virial and projected masses for the Sombrero of  $M_{\text{VT}} = (8.1 \pm 1.8) \times 10^{11} M_{\odot}$  and  $M_{\text{P}} = (5.3 \pm 1.0) \times 10^{11} M_{\odot}$  within 17 kpc, respectively. Using 12 clusters within the central 4.5 kpc the corresponding numbers are  $M_{\text{VT}} = (2.1 \pm 1.1) \times 10^{11} M_{\odot}$  and  $M_{\text{P}} = (2.0 \pm 1.3) \times 10^{11} M_{\odot}$ .

*Subject headings:* galaxies: star clusters — galaxies: abundances — galaxies: halos — galaxies: bulges — galaxies: individual (NGC 4594)

---

<sup>1</sup>Based on data obtained at the W.M. Keck Observatory, which is operated as a scientific partnership among the California Institute of Technology, the University of California and the National Aeronautics and Space Administration.

## 1. Introduction

The Sombrero galaxy (M104 = NGC 4594) is well known for its dominating bulge/halo component which contributes with about 80% of the total luminosity (Kent 1988; Baggett, Baggett & Anderson 1998). This makes the Sombrero an important intermediary case between later-type spirals and elliptical/S0 galaxies, and an ideal place to study the relation between spiral bulges and early-type galaxies. One interesting aspect of such studies is to compare the globular cluster (GC) systems of early- and late-type galaxies. The Sombrero has a very rich GC system with an estimated total of  $\sim 2000$  clusters (Harris et al. 1984; Bridges & Hanes 1992; Forbes, Grillmair & Smith 1997), about an order of magnitude more than the Milky Way and M31 (Harris 1996; Fusi Pecci et al. 1993), but comparable to many early-type galaxies of the same luminosity. Using archive WFPC2 images, Larsen, Forbes & Brodie (2001, hereafter Paper I) detected a clearly bimodal color distribution for the Sombrero GCs, confirming hints by Forbes, Grillmair & Smith (1997). The number of red (metal-rich) and blue GCs were found to be roughly equal, in contrast to M31 and the Milky Way where the metal-poor GCs constitute about  $2/3 - 3/4$  of the total population, but again similar to the situation in early-type galaxies. Thus, we suggested in Paper I that the metal-rich GCs in the Sombrero are associated with the bulge rather than with its disk, in which case a much more modest number of metal-rich GCs would have been expected. The WFPC2 data presented in Paper I also showed that the mean colors of the two GC populations in the Sombrero are very similar to those in early-type galaxies as well as the Milky Way, M31 and other spiral galaxies (Forbes, Brodie & Larsen 2001), with inferred mean metallicities of  $[\text{Fe}/\text{H}] \sim -1.40$  and  $-0.54$ .

Although there may not be a one-to-one correspondence between star formation and formation of globular clusters, information about the age distribution of GCs would presumably provide valuable insight about major star formation episodes in their host galaxies. An important, unresolved issue is whether age differences exist between the GC subpopulations in galaxies, and how large such age differences might be. This question is still controversial even in our Galaxy, where GC ages can be derived from color-magnitude diagrams (Stetson, Vandenberg, & Bolte 1996; Buonanno et al. 1998; Rosenberg et al. 1999), so it is not surprising that it has proven to be very difficult to obtain reliable information about ages of extragalactic GCs from integrated photometry and/or spectroscopy. As shown by de Freitas Pacheco & Barbuy (1995), blue horizontal-branch morphology can have a significant impact on observed  $\text{H}\beta$  indices, the most commonly used age indicator. More recently, Schiavon et al. (2002) have discussed a number of problems in the modeling of globular cluster spectra, and concluded that uncertainties in the luminosity function of the red and asymptotic giant branches,  $\alpha$ -element enhancement, horizontal branch morphology and other factors can affect spectroscopic age estimates by at least 3–4 Gyr. Observationally, useful constraints on typical GC ages require very accurate measurements of Balmer line indices, as the separation between e.g. the 10 Gyr and 11 Gyr isochrones is only about  $0.1 \text{ \AA}$  in the equivalent width of  $\text{H}\beta$ . Furthermore, at lower metallicities ( $[\text{Fe}/\text{H}] \lesssim -1$ ), recent models (Maraston 2001, priv. comm., Bruzual & Charlot 2001, priv. comm.) suggest that the Balmer lines no longer depend on age in a

simple way for ages greater than about 10 Gyr.

A more indirect way to constrain the formation history of stellar populations in general, including GCs, is by studying their abundance patterns. The Milky Way bulge and halo populations, as well as many early-type galaxies, show an enhancement in the abundances of  $\alpha$ -elements relative to the Fe-group compared to the Sun (van den Bergh 1995, and references therein). The enhancement is typically around  $[\alpha/\text{Fe}] \sim +0.3$  (Carney 1996) and is also seen in the Sombrero bulge stars (Peletier et al. 1999). The most commonly adopted explanation is that different elements are produced by stars with different lifetimes, of which supernovae of type Ia are generally assumed to have the longest lifetimes and make the strongest contribution to Fe. Thus, populations that formed on time-scales too short for SN Ia to have made any significant contribution to the abundance patterns show “enhancement” of other elements relative to Fe (e.g. Tinsley 1979). Therefore, studies of abundance patterns may provide an alternative chronometer for the chemical evolutionary history of galaxies, although the timescale for development of SN Ia remains very uncertain.

Because of its relatively small distance and rich GC system, the Sombrero galaxy is an attractive target for detailed studies of individual GCs. With 8–10 m class telescopes, high-quality spectra can be obtained for many of the brighter clusters, and by co-adding spectra of several GCs it is possible to achieve sufficient S/N to bring the errors down to a level where model uncertainties rather than observational errors dominate. This makes it possible to test whether the models yield internally consistent results, e.g. by comparing age estimates based on different Balmer lines ( $H\beta$ ,  $H\gamma$ ,  $H\delta$ ).

Spectroscopically, the GC system of the Sombrero has been studied by Bridges et al. (1997) who obtained rather low S/N spectra for 34 confirmed GCs. By co-adding the spectra they found a mean metallicity of  $[\text{Fe}/\text{H}] = -0.70 \pm 0.3$ , but the S/N was too low to constrain metallicities of individual clusters. In this paper we present new spectra for GCs in the Sombrero, selected from the Paper I sample. Of 17 GC candidates, 14 are confirmed as GCs. Combining our data with those of Bridges et al. (1997), the total number of confirmed GCs in the Sombrero is increased to 48. The best of our spectra have a S/N of about 50 per pixel, allowing us to accurately measure the metallicities of individual clusters and compare with previous photometric estimates. By co-adding the spectra of blue (metal-poor) and red (metal-rich) clusters, we also put constraints on the ages (Section 4.2) and abundance ratios (Section 4.3) of the Sombrero GC subpopulations. Finally, we use all available GC radial velocities in the Sombrero to constrain the mass of the Sombrero galaxy (Section 5).

## 2. Data

The data were obtained with the LRIS spectrograph (Oke et al. 1995) on the Keck I telescope during two observing runs on 2001, April 28 and May 19–20. We utilized the newly installed blue side on LRIS (“LRIS-B”) and a dichroic splitting at 5600Å to simultaneously obtain blue and red

spectra, covering the regions  $\sim 3500\text{--}5500\text{\AA}$  and  $\sim 5700\text{--}8500\text{\AA}$ , respectively. On the blue side a 400 l/mm grism was used, providing a dispersion of  $1.74\text{\AA pix}^{-1}$  and a resolution of  $\sim 8\text{\AA}$ . On the red side we used a 600 l/mm grating blazed at  $5000\text{\AA}$ , with a dispersion of  $1.28\text{\AA pix}^{-1}$  and a resolution of  $\sim 6\text{\AA}$ . In addition to the multislit spectra of Sombrero GC candidates, we also obtained long-slit spectra for a number of radial velocity standard stars, flux standards, and Lick/IDS standard stars from Worthey et al. (1994).

Because of anticipated problems with “ghosts” in LRIS-B, we applied  $2''$  offsets to the telescope pointing for some exposures. Although these offsets were intended to be parallel to the slitlets, we found that they inevitably included some component perpendicular to the slits as well, resulting in greatly reduced signal from our science targets. Thus, we quickly decided to abandon this procedure. Another problem was related to the input coordinates. For the April run we used coordinates measured directly on the “central” and “inner halo” WFPC2 images from Paper I, using the METRIC task in the STSDAS package. Unfortunately, there were systematic differences between the two WFPC2 pointings which made it impossible to align all objects in the slitlets at the same time. For the May run we used direct images from the April run to alleviate this problem, but as a result of these slitmask alignment problems, we achieved a significantly lower S/N for some of the objects than could have been possible under optimal circumstances.

Following initial processing of the images (bias subtraction, flatfielding), the spectra were extracted using standard tools in the IRAF SPECRED package<sup>2</sup>. As the spectra were obtained over several hours, significant shifts in the wavelength scale due to mechanical flexure were found to be present between individual integrations, amounting to up to  $\approx 5\text{\AA}$ . Assuming that all spectra in a given exposure were subject to the same shifts, the shifts were determined by cross-correlating the spectra of the brightest objects in each exposure with the spectra in a reference exposure, taken immediately before the arc spectra. For the red spectra, the wavelength zero-point was further fine-tuned using the NaD night sky lines at  $\lambda\lambda 5890$  and  $5896\text{\AA}$ . Finally, the individual spectra of each object were co-added, using a sigma-clipping algorithm to reject cosmic ray events. The S/N at each pixel in the combined spectra was estimated from the variance of the combined pixels. The total integration time was  $5\frac{1}{2}$  hours.

Table 1 lists all science objects for which spectra were obtained. The object IDs refer to Paper I, where the coordinates are listed. For convenience, we have also included the  $V, I$  photometry from Paper I. Note that the brightest cluster, H2-22, was saturated on the WFPC2 data used in Paper I, making its  $V-I$  color unreliable. The radial velocities in Table 1 are generally measured on the red spectra, for which the wavelength calibration zero-point could be checked using the night sky lines. The errors on the radial velocities in Table 1 are random errors, based on the uncertainties in the location of the cross-correlation peak reported by the FXCOR task. These do not take into account various systematic errors, mostly due to uncertainties in wavelength calibration. We

---

<sup>2</sup>IRAF is distributed by the National Optical Astronomical Observatories, which are operated by the Association of Universities for Research in Astronomy, Inc. under contract with the National Science Foundation

estimate that such errors are on the order  $\sim 0.5\text{\AA}$ , or  $\sim 25$  km/s. No skylines were present in the blue spectra, and differences of 100–150 km/s between radial velocities measured on the blue and red spectra were not uncommon. Another problem with the wavelength calibration in the blue stems from the fact that the calibration lamps in LRIS only had a few (5–7) suitable lines. The best fitting 2nd order polynomial wavelength solutions in the blue generally had a significant residual scatter (1–2 $\text{\AA}$ ), presumably indicating that higher-order terms ought to be included in the wavelength solution, but the small number of calibration lines made it impossible to include higher-order terms.

The radial velocity of the Sombrero galaxy is listed as 1024 km/s in the RC3 catalogue (de Vaucouleurs et al. 1991). If we exclude the three objects in Table 1 with  $RV < 600$  km/s, we are left with a sample of 14 globular clusters. These have a mean radial velocity of 1019 km/s and a dispersion of 246 km/s, in excellent agreement with the radial velocity of the Sombrero itself. Of the three objects with radial velocities less than 600 km/s, two (H2-06 and H2-10) are very compact and essentially unresolved on the HST images with effective radii  $\lesssim 0.3$  pc (Larsen, Forbes & Brodie 2001) and are most likely foreground stars. The third (H2-27) is quite well-resolved on the HST images and has an effective radius of 3.4 pc, typical for globular clusters. It therefore seems likely that this object is indeed a globular cluster. The S/N of this spectrum is very poor and the cross-correlation signal was not very strong, so the radial velocity may be in error. In fact, using the blue spectrum of this object, we get a radial velocity of 1069 km/s. Because of the uncertain radial velocity and poor S/N we exclude this object from further analysis in this paper.

Before spectrophotometric indices were measured, the spectra must be corrected for radial velocity. Rather than blindly applying the radial velocities in Table 1 to the blue spectra, we used a number of easily identifiable features such as the  $H\beta$ ,  $H\gamma$ ,  $H\delta$ , Ca II H+K lines and the G-band to determine small zero-point shifts and scale corrections to the dispersion solutions. Thus, the wavelength scale of the final spectra used for the spectrophotometric analysis was typically accurate to better than 1 $\text{\AA}$  in the region of interest (i.e.  $\sim 3700$ – $5400$   $\text{\AA}$ ).

### 3. Measuring Lick/IDS indices on LRIS-B spectra

In order to test if there might be any systematic differences between indices measured on LRIS-B spectra and the standard Lick/IDS system, we observed a number of stars from Worthey et al. (1994) in longslit mode. In Fig. 1 we compare our LRIS-B measurements of all Lick/IDS indices that were covered by our blue spectra with the standard values. Generally, our measurements agree well with the standard values, although there are slight systematic offsets for some of the narrower indices like Ca4227 and Ca4455. This may be attributed to the slightly higher resolution of LRIS-B compared to the Lick/IDS spectrograph.

Unfortunately, the wavelength range covered in longslit mode by LRIS is slightly different from the one covered in multislit mode and does not extend beyond 5300 $\text{\AA}$ . Therefore, several key indices

(such as  $Mg_2$ , Fe5270 and Fe5335) redward of this limit could not be compared. Furthermore, since this part of the spectrum is not covered by the flux standards, the flux calibration of the multislit spectra beyond  $5300\text{\AA}$  also becomes uncertain. This is particularly problematic because the blue reflection efficiency of the dichroic already begins to drop around  $\sim 5300\text{\AA}$ .

## 4. Constraining ages and metallicities

### 4.1. Metallicities

We derived metallicities for each GC using the calibration by Brodie and Huchra (1990), but adopting the modification to the error on the combined metallicity estimate described in Larsen and Brodie (2000). Metallicities for each of the individual calibrators, as well as the combined metallicity estimates are listed in Table 2. For comparison we have also included photometric metallicities based on the  $V-I$  colors in Table 1 and the calibration in Kissler-Patig et al. (1998). The spectroscopic and photometric metallicity estimates are compared in Fig. 2 and generally agree quite well. Three representative globular cluster spectra with low, intermediate and high metallicities are shown in Fig. 3.

### 4.2. Comparison with population synthesis models

High S/N spectra have the potential to remove the age-metallicity degeneracy inherent in photometric studies. At least in principle, ages are well constrained by Balmer line strengths, while metallicity information is provided by indices such as Fe5270, Fe5335 and  $Mg_2$  (Worthey 1994).

Here we compare our Sombrero spectra with two sets of recent population synthesis models, kindly provided by C. Maraston (see Maraston & Thomas 2000) and R. Schiavon (Schiavon et al. 2002b). Like most of the current models, the Maraston models are based on the “fitting” functions by Worthey et al. (1994). The Schiavon models are based on a new set of fitting functions derived from the spectral library of Jones (1999), and also include empirical corrections to the luminosity function of red giants (Schiavon et al. 2002). We use a preliminary version of the Schiavon models where only the Balmer line indices are based on the new fitting functions, i.e. other indices such as  $Mgb$ ,  $Mg_2$  and the various Fe indices are still based on the Worthey fitting functions. The Schiavon models also cover a more limited age/metallicity range than the Maraston models, but the comparison nevertheless provides some useful insight into the differences between various available models. As discussed in Sect 3, our instrumental system appears to be very similar to the Lick/IDS system so we have not applied any corrections to spectrophotometric indices measured on the LRIS-B spectra.

As mentioned earlier, some indices may be compromised by difficulties with the calibration of the blue spectra redward of  $5300\text{\AA}$ . The  $Mg_2$  index is particularly vulnerable to such problems

because of the wide separation between the continuum passbands, and offsets are frequently found between the standard Lick/IDS indices and instrumental systems (e.g. Kuntschner 2000). In Fig. 4 we compare our measurements of  $Mg_2$  with  $Mgb$ , which is slightly narrower but measures essentially the same feature. However, while the continuum passbands of  $Mg_2$  are located about  $150\text{\AA}$  from the feature passband, those of  $Mgb$  are located adjacent to it, making  $Mgb$  much less sensitive to errors in the continuum slope. Generally, Fig. 4 shows that the two Mg sensitive indices correlate well, but the slope of our observed  $Mgb$ – $Mg_2$  relation is shallower than the Maraston model predictions, which in turn agree well with  $Mgb$ – $Mg_2$  plots in e.g. Trager et al. (1998) and Beasley et al. (2000). One possible explanation for this discrepancy is that errors in the continuum level at the position of the red continuum passband cause us to measure too low values for the  $Mg_2$  index because of uncorrected reduced throughput by the dichroic. Another possibility is that peculiarities in the abundance patterns affect the continuum passbands of  $Mgb$  and  $Mg_2$  in different ways (Tripicco & Bell 1995).

In Fig. 5 we compare various index measurements with the Maraston and Schiavon model predictions. The Schiavon models are tabulated at 5, 7.9, 11.2 and 14.1 Gyr and at metallicities of  $[Fe/H] = -0.7, -0.4, 0.0$  and  $+0.2$ . While the Maraston models are tabulated at 1 Gyr intervals from 2 to 15 Gyrs, we have plotted only the 5, 8, 11 and 14 Gyr models, for easy comparison with the Schiavon models. Note that the metallicity divisions of the Maraston models are different from those of the Schiavon models ( $[Fe/H] = -2.25, -1.35, -0.33, 0.00$  and  $+0.35$ ). Panels (a) and (b) show  $H\beta$  vs.  $\langle Fe \rangle$  and the  $Mgb$  index, where  $\langle Fe \rangle = (Fe5270 + Fe5335)/2$ . The Maraston and Schiavon model grids are shown with solid lines and dashed lines, respectively. In panels (c) and (d) we show  $H\gamma_A$  and  $H\delta_A$  vs.  $\langle Fe \rangle$ , using the definitions in Worthey & Ottaviani (1997). Because of the difficulties with the calibration of  $Mg_2$  discussed earlier, we have chosen  $Mgb$  instead of  $Mg_2$  even though the formal errors on  $Mgb$  are somewhat larger. The errors on the indices were estimated directly from the S/N of the spectra.

To first order, Fig. 5 indicates high ages for most clusters, although the error bars are generally still too large to put strong constraints on the ages of individual clusters. In order to compare the mean properties of metal-rich and metal-poor GCs, we therefore co-added all spectra with  $[Fe/H] < -1$  and  $[Fe/H] > -1$ , respectively. The co-added spectra are shown in Figure 6 and the corresponding datapoints are shown with filled circles in Fig. 5. In the  $H\beta$  plots both the metal-poor and metal-rich co-added datapoints fall near the  $\sim 11$  Gyr Maraston isochrones, with little evidence of any significant age differences between the two within the formal  $\sim 2$  Gyr error bars on the co-added data. The Schiavon models tend to predict lower ages for a given  $H\beta$  index than the Maraston models, especially at younger ages and lower metallicities. At the location of the metal-rich Sombrero GCs in the  $\langle Fe \rangle$ – $H\beta$  plane the difference is relatively modest and amounts to an age difference of only 1–2 Gyrs, but at lower metallicities the difference between the two sets of models becomes more pronounced and amounts to about 4 Gyrs at the lowest metallicity tabulated by Schiavon. Thus, the trend in these models is to decrease the ages of the metal-poor clusters more than those of the metal-rich ones, relative to the Maraston models.

The  $H\gamma_A$  and  $H\delta_A$  measurements basically confirm the ages estimated from  $H\beta$ , but note that both  $H\gamma_A$  and  $H\delta_A$  reach a minimum around 11 Gyr at low metallicities and then increase strongly at higher ages. At  $[\text{Fe}/\text{H}] = -1.35$ , the Maraston models predict about the same  $H\gamma_A$  and  $H\delta_A$  strengths at 15 and 5 Gyrs. The Schiavon models do not include tabulations of  $H\gamma_A$  and  $H\delta_A$ , but in Figure 7 we show their predictions for another  $H\gamma$  index defined by Vazdekis et al. (2001). This  $H\gamma$  index (in the following denoted  $H\gamma_{\text{vaz}}$ ) differs from  $H\gamma_A$  in that the continuum passbands are located closer to the feature passband, thereby avoiding the strong metallicity dependence of  $H\gamma_A$  which results from its blue continuum passband coinciding with the G-band. In fact, Figure 7 shows that  $H\gamma_{\text{vaz}}$  is practically independent of metallicity, at least within the range spanned by the models. Taken at face value, Figure 7 would suggest that the metal-rich clusters are slightly *older* than the metal-poor ones, but both sub-populations are compatible with the same (high) age within the errors. Thus, although it should be stressed that even relative ages may still be somewhat model-dependent, it seems reasonable to conclude that both GC sub-populations in the Sombrero are old, and probably coeval to within the measurement uncertainties, i.e. with age differences of 2–3 Gyrs at most.

### 4.3. Abundance ratios

Some attempts to model the effect of  $\alpha$ -element enhancement on Lick indices have been made by Milone, Barbuy, & Schiavon (2000), who modeled the effect of  $\alpha$ -element enhancement on the Lick  $\text{Mg}_2$  index and a broad index ( $\text{TiO}_{12.5}$ ) covering the TiO band centered at 7257 Å. The  $\text{TiO}_{12.5}$  index is included in our red LRIS spectra. Because of the problems with the calibration of  $\text{Mg}_2$ , we converted the Milone et al. model predictions for  $\text{Mg}_2$  to  $\text{Mgb}$ , using the Maraston models. We found that the linear relation  $\text{Mgb} = 14.03 \text{Mg}_2 + 0.361$  approximated the Maraston models to within 0.1 Å for the age range 10–15 Gyr and  $\text{Mg}_2 < 0.3$  (Fig. 4).

In addition to the strong terrestrial  $\text{O}_2$  absorption bands, which are located just outside the  $\text{TiO}_{12.5}$  continuum passbands, the wavelength region around 7200–7500 Å is affected by terrestrial  $\text{H}_2\text{O}$  absorption. We corrected our red spectra for this by normalizing the flux standard spectra with a smooth continuum and then dividing the GC spectra by the normalized flux standard spectra. This correction affected the  $\text{TiO}_{12.5}$  index downwards by about 7 Å. Fig. 8 shows our measurements of  $\text{TiO}_{12.5}$  and  $\text{Mgb}$  on the co-added spectra, compared to the alpha-enhanced models by Milone, Barbuy, & Schiavon (2000). In the  $\langle \text{Fe} \rangle - \text{Mgb}$  plot we also show the Maraston models for an age of 12 Gyr. Note that the most metal-poor Maraston models are actually rather similar to the  $[\alpha/\text{Fe}] = +0.3$  models by Milone, Barbuy, & Schiavon (2000), but approach the  $[\alpha/\text{Fe}] = 0$  models at higher metallicities. This is probably because many of the metal-poor stars used to set up the Worthey fitting functions are alpha-enhanced (Maraston & Thomas 2000). For the metal-rich Sombrero GCs, both  $\text{Mgb}$  and  $\text{TiO}_{12.5}$  indicate clearly supersolar  $[\alpha/\text{Fe}]$  ratios around  $[\alpha/\text{Fe}] \sim +0.4$ . For the metal-poor clusters, the  $\text{TiO}_{12.5}$  index again indicates supersolar  $[\alpha/\text{Fe}]$  ratios similar to those of the metal-rich clusters, although the  $\text{Mgb}$  plot actually suggests  $[\alpha/\text{Fe}]$

closer to 0 for the metal-poor clusters. However, at low metallicities the separation between the different  $[\alpha/\text{Fe}]$  models is smaller and it seems most likely that both the metal-poor and metal-rich GCs in the Sombrero have super-solar  $[\alpha/\text{Fe}]$  ratios similar to those observed in Milky Way GCs, the bulge of the Sombrero and in early-type galaxies.

## 5. Mass of the Sombrero

Globular clusters can be used as tracers of the mass of their host galaxy, as demonstrated e.g. by Huchra & Brodie (1987) (for M87) and Kissler-Patig et al. (1998) (NGC 1399). We combined our data in Table 1 with data for 34 Sombrero GCs from Bridges et al. (1997). Our sample does not overlap with that of Bridges et al. (1997), so by combining theirs and our data we get a total of 48 GCs.

Fig. 9 shows the radial velocities as a function of the offset in R.A. from the center of the Sombrero (the major axis is aligned roughly east-west). Bridges et al. (1997) found hints of rotation in the cluster system, but our data clearly do not add much to the significance of their result. For completeness we also plot the radial velocities for the metal-rich and metal-poor clusters from our sample separately, but the data are clearly insufficient to provide any constraints on rotation in either sample.

Following Huchra & Brodie (1987), we can use the GC radial velocities to obtain a mass estimate for the Sombrero in two ways. The virial mass is estimated as

$$M_{\text{VT}} = \frac{3\pi N}{2G} \frac{\sum_i^N V_i^2}{\sum_{i<j} 1/r_{ij}} \quad (1)$$

and the projected mass is

$$M_P = \frac{f_p}{GN} (\sum_i^N V_i^2 r_i) \quad (2)$$

In these equations,  $r_{ij}$  is the distance between the  $i$ th and  $j$ th clusters,  $r_i$  is the distance between the  $i$ th cluster and the galaxy center and  $V_i$  is the velocity difference between the  $i$ th cluster and the mean system velocity.  $N$  is the number of clusters. The value of  $f_p$  depends on the cluster orbits; following Bridges et al. (1997) we adopt  $f_p = 16/\pi$  for isotropic orbits.

For the total sample of 48 clusters we get  $M_{\text{VT}} = (8.1 \pm 1.8) \times 10^{11} M_\odot$  and  $M_P = (5.3 \pm 1.0) \times 10^{11} M_\odot$  within 17 kpc, adopting a distance of 8.7 Mpc (Larsen, Forbes & Brodie 2001). Using only our 14 clusters, we get  $M_{\text{VT}} = (3.2 \pm 1.5) \times 10^{11} M_\odot$  and  $M_P = (4.2 \pm 2.1) \times 10^{11} M_\odot$  (within 13 kpc). For comparison, Bridges et al. (1997) got  $M_P = 5.2_{3.9}^{6.7} \times 10^{11} M_\odot$ . The 12 clusters in the central HST pointing are useful as probes of the mass located within the central regions of the galaxy, and yield  $M_{\text{VT}} = (2.1 \pm 1.1) \times 10^{11} M_\odot$  and  $M_P = (2.0 \pm 1.3) \times 10^{11} M_\odot$  within the central 4.5 kpc. The errors were estimated by a standard “jackknife” procedure.

## 6. Summary and conclusions

We have analyzed Keck / LRIS-B spectra for 17 globular cluster (GC) candidates in the Sombrero galaxy, of which 14 are confirmed as true GCs based on their radial velocities. One additional object has too low S/N for reliable radial velocity measurements, but based on the HST images presented by Larsen, Forbes & Brodie (2001) it is probably also a GC. We find generally good agreement between spectroscopic metallicities and previous photometric metallicities based on  $V-I$  colors. Comparison of Lick/IDS indices with population synthesis models indicates that both the metal-rich and metal-poor clusters are 10–15 Gyr old, with preferred ages around 11–12 Gyr. We see no detectable age differences between the two GC populations, although differences of a few Gyrs cannot be ruled out. Comparison of  $\langle \text{Fe} \rangle$ ,  $\text{Mgb}$  and  $\text{TiO}$  indicates that the Sombrero GCs probably have super-solar  $[\alpha/\text{Fe}]$  ratios  $\sim +0.4$ , similar to or perhaps slightly larger than those observed in Milky Way globular clusters.

Overall, the Sombrero GC system shares many similarities with that of the Milky Way, as well as many early-type galaxies. With few exceptions, both GC populations generally appear to be old, and another common feature seems to be an enhancement in  $\alpha$ -element abundances, probably indicating that the gas out of which the clusters formed was enriched predominantly by type-II supernovae. This suggests that the majority of GCs formed early on, before type Ia SNe made a significant contribution to chemical enrichment, and presumably within a few Gyrs after star formation commenced. The metal-rich GCs in the Sombrero, like those in most galaxies, probably formed early on when galaxies were still assembling with high star formation rates and gas densities providing favorable conditions for the formation of large numbers of massive star clusters. The metal-poor clusters might have formed even earlier at high redshifts, triggered by ionization fronts (Cen 2001).

Finally, we combine our sample with data for 34 GCs from Bridges et al. (1997) and obtain virial and projected masses for the Sombrero of  $M_{\text{VT}} = (8.1 \pm 1.8) \times 10^{11} M_{\odot}$  and  $M_{\text{P}} = (5.3 \pm 1.0) \times 10^{11} M_{\odot}$ , respectively. This is in good agreement with previous estimates of the mass of the Sombrero. For 12 clusters located within the central 4.5 kpc (projected) we estimate  $M_{\text{VT}} = (2.1 \pm 1.1) \times 10^{11} M_{\odot}$  and  $M_{\text{P}} = (2.0 \pm 1.3) \times 10^{11} M_{\odot}$ .

This work was supported by National Science Foundation grant number AST9900732. We are grateful to Dr. Andre Milone for providing his  $\alpha$ -enhanced models in electronic form and to Dr. Ricardo Schiavon for allowing us to use his population models prior to publication. Helpful comments by an anonymous referee are appreciated. MB thanks the Royal Society of London for their support.

## REFERENCES

- Baggett W. E., Baggett S. M., Anderson K. S. J., 1998, *AJ*, 116, 1626
- Beasley, M. A., Sharples, R. M., Bridges, T. J., Hanes, D. A., Zepf, S. E., Ashman, K. M., & Geisler, D. 2000, *MNRAS*, 318, 1249
- Bridges T. J., Hanes D. A., 1992, *AJ*, 103, 800
- Bridges T. J., et al., 1997, *MNRAS*, 284, 376
- Brodie, J. P. and Huchra, J. P. 1990, *AJ*, 362, 503
- Bruzual, G. A. and Charlot, S. 2001, in preparation
- Buonanno, R., Corsi, C. E., Pulone, L., Fusi Pecci, F., & Bellazzini, M. 1998, *A&A*, 333, 505
- Carney, B. W. 1996, *PASP*, 108, 900
- Cen, R., *ApJ*, 560, 592
- de Freitas Pacheco, J. A. & Barbuy, B. 1995, *A&A*, 302, 718
- de Vaucouleurs, G., de Vaucouleurs, A., Corwin Jr., H. G. et al. 1991, *Third Reference Catalogue of Bright Galaxies, Version 3.9 (RC3)*
- Forbes, D. A., Brodie, J. P., & Larsen, S. S. 2001, *ApJ*, 556, L83
- Forbes D. A., Grillmair C. J., Smith R. C., 1997, *AJ*, 113, 1648
- Fusi Pecci, F., Cacciari, C., Federici, L., & Pasquali, A. 1993, *ASP Conf. Ser. 48: The Globular Cluster-Galaxy Connection*, 410, editors: G. H. Smith and J. P. Brodie
- Harris W. E., Harris H. C., Harris G. L. H., 1984, *AJ*, 89, 216
- Harris, W. E. 1996, *AJ*, 112, 1487
- Huchra, J. & Brodie, J. 1987, *AJ*, 93, 779
- Jones, L. A. 1999, *PhD Thesis, University of North Carolina*
- Kent, S. M., 1988, *AJ*, 96, 514
- Kissler-Patig, M., Brodie, J. P., Schroder, L. et al., 1998, *AJ*, 115, 105
- Kuntschner, H. 2000, *MNRAS*, 315, 184
- Larsen, S. S., and Brodie, J. P., 2002, *AJ*, in press
- Larsen, S. S., Forbes, D. A., Brodie, J. P., 2001, *MNRAS*, 327, 1116 (PaperI)

- Maraston, C. & Thomas, D. 2000, *ApJ*, 541, 126
- Milone, A., Barbuy, B., & Schiavon, R. P. 2000, *AJ*, 120, 131
- Oke, J. B. Cohen, J. G., Carr, M. et al. 1995, *PASP*, 107, 375
- Peletier, R. F., Vazdekis, A., Arribas, S., del Burgo, C., García-Lorenzo, B., Gutiérrez, C., Mediavilla, E., & Prada, F. 1999, *MNRAS*, 310, 863
- Rosenberg, A., Saviane, I., Piotto, G., & Aparicio, A. 1999, *AJ*, 118, 2306
- Schiavon, R. P., Faber, S. M., Rose, J. A., Castilho, B. V., 2002, *AJ*, submitted (astro-ph/0109365)
- Schiavon, R. P., et al., 2002, in preparation
- Stetson, P. B., Vandenberg, D. A., & Bolte, M. 1996, *PASP*, 108, 560
- Tinsley, B. M. 1979, *ApJ*, 229, 1046
- Trager, S. C., Worthey, G., Faber, S. M., Burstein, D., & Gonzalez, J. J. 1998, *ApJS*, 116, 1
- Tripicco, M. J. & Bell, R. A. 1995, *AJ*, 110, 3035
- van den Bergh, S. 1995, *ApJ*, 450, 27
- Vazdekis, A., Salaris, M., Arimoto, N., & Rose, J. A. 2001, *ApJ*, 549, 274
- Worthey, G., 1994, *ApJS*, 95, 107
- Worthey, G., Faber, S. M., González, J. J., and Burstein, D. 1994, *ApJS*, 94, 687
- Worthey, G. & Ottaviani, D. L. 1997, *ApJS*, 111, 377

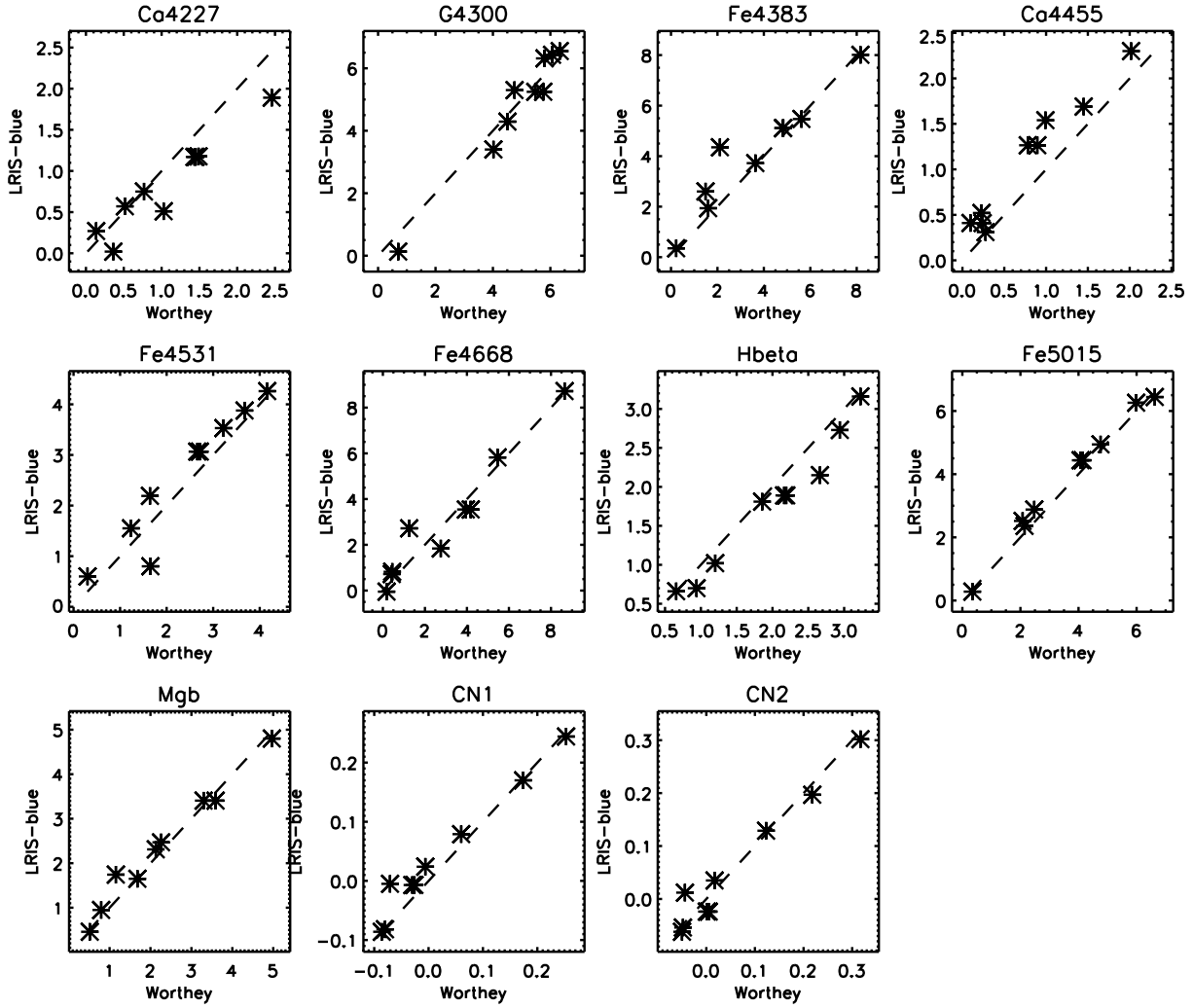


Fig. 1.— Lick/IDS indices measured on our LRIS-B spectra, compared to standard values from Worthey et al. (1994). The agreement is generally good, except for narrow indices like Ca4227 and Ca4455.

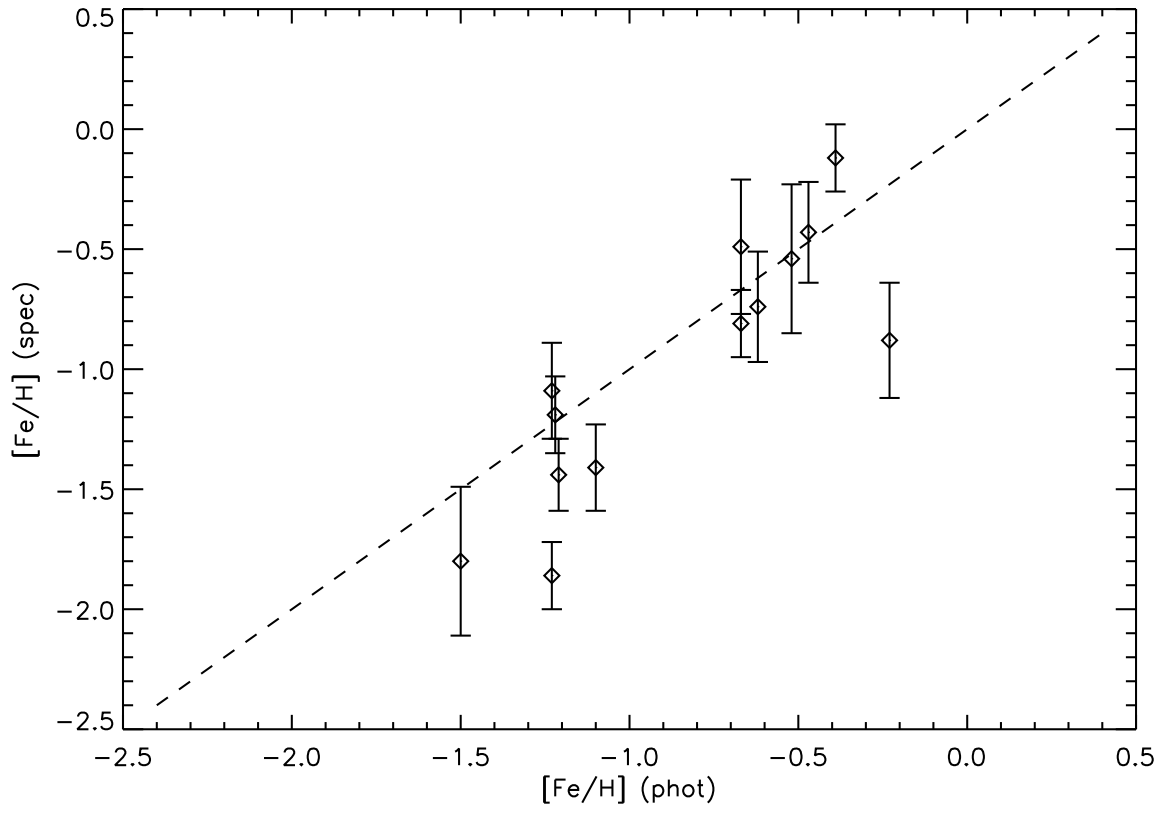


Fig. 2.— Comparison of spectroscopic and photometric metallicity estimates for Sombrero GCs.

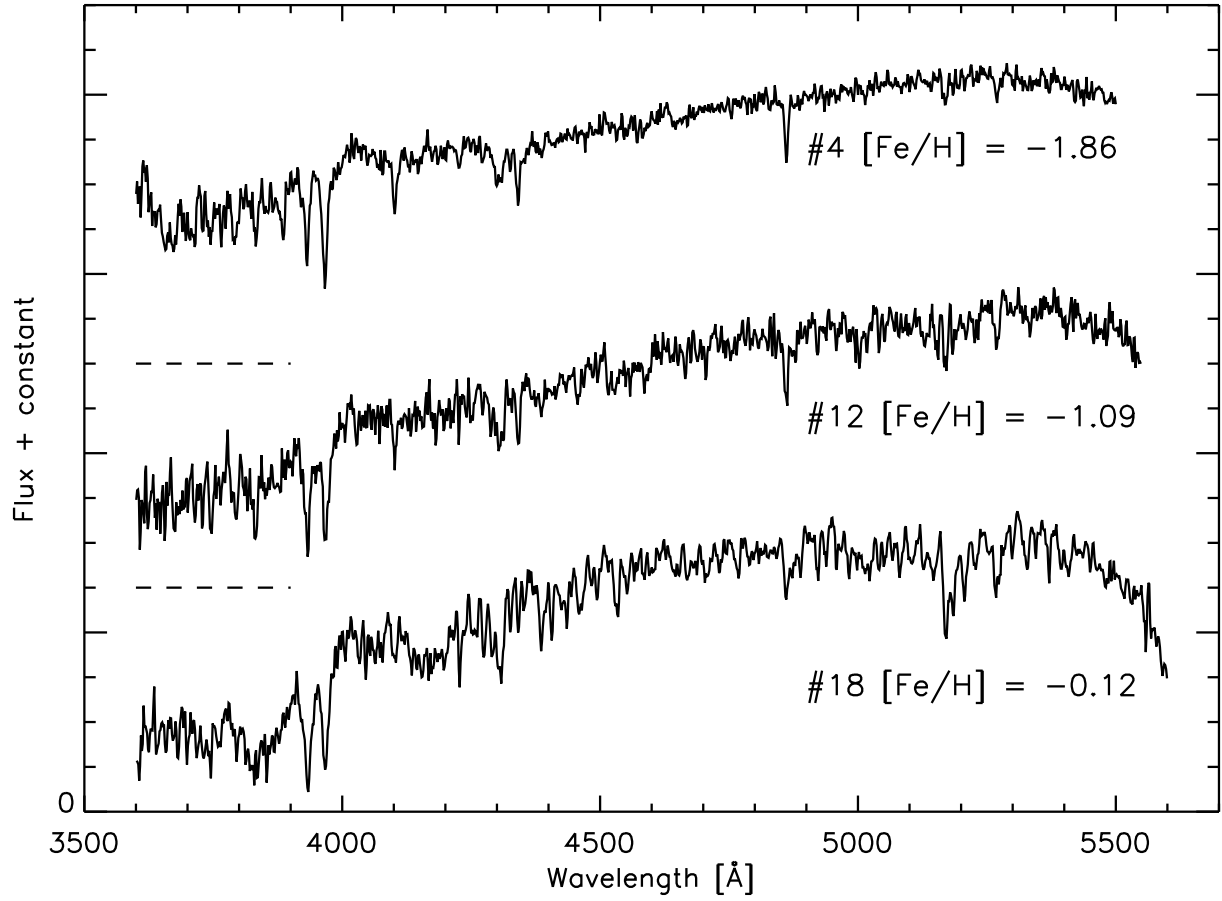


Fig. 3.— Spectra for three globular clusters with low (top), moderate (center) and high (bottom) metallicities. Note: no smoothing has been done. The two upper spectra have been shifted for clarity, with the zero-levels indicated by the short dashed lines.

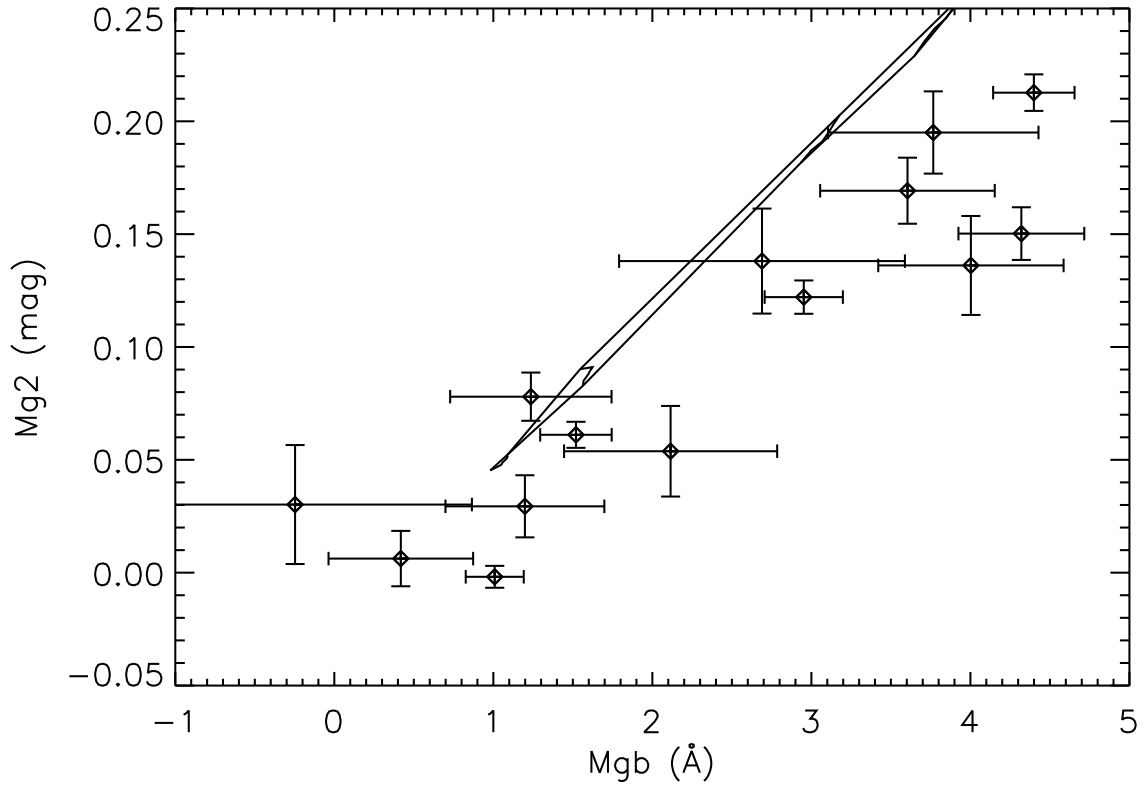


Fig. 4.— Comparison of  $Mgb$  and  $Mg_2$  for Sombrero GCs. Maraston models for 10 and 15 Gyr are overplotted on the figure.

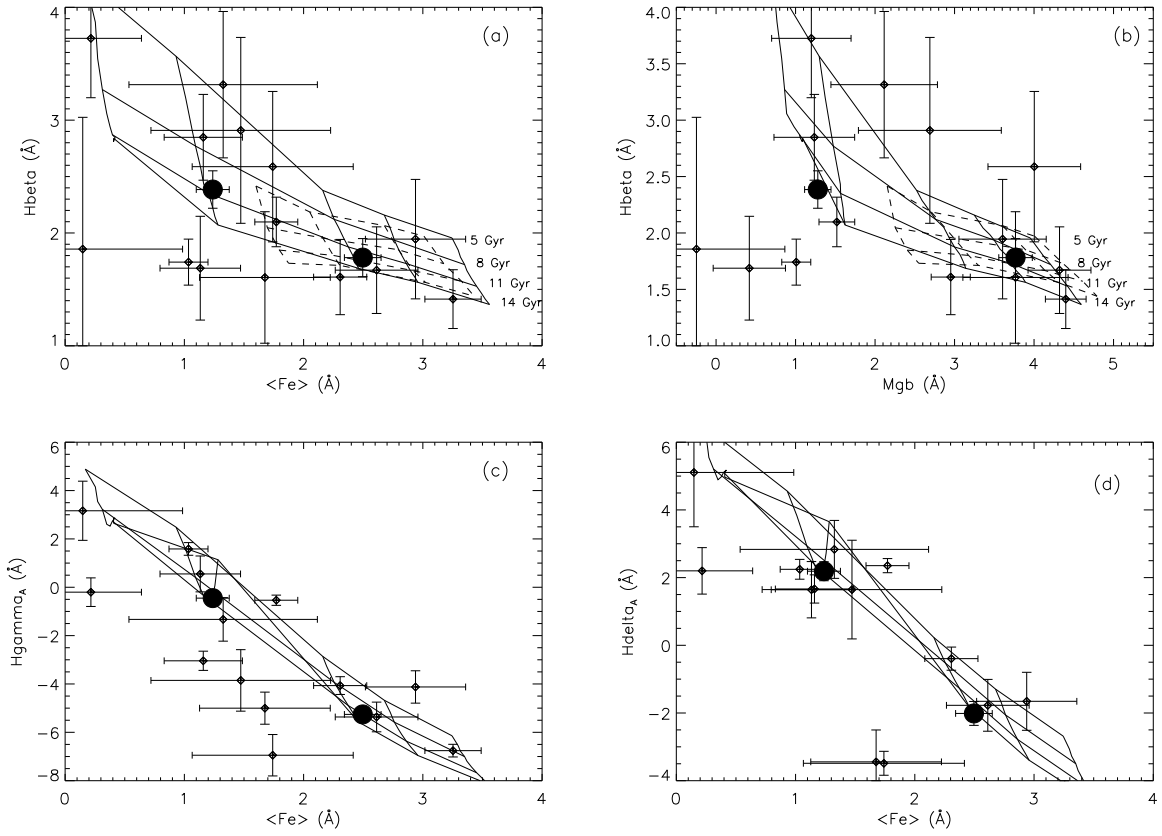


Fig. 5.— Comparison of our data with population synthesis models by C. Maraston and R. Schiavon. Panels (a) and (b):  $\langle \text{Fe} \rangle$  and  $Mgb$  vs.  $H\beta$ . Panels (c) and (d):  $\langle \text{Fe} \rangle$  vs.  $H\gamma_A$  and  $H\delta_A$ . Maraston models (solid line grids) are shown for ages of 5, 8, 11 and 14 Gyr and  $[\text{Fe}/\text{H}] = -2.25, -1.35, -0.33, 0.0$  and  $+0.35$ . Schiavon models (dashed line grids) are for ages of 5, 7.9, 11.2 and 14.1 Gyr and  $[\text{Fe}/\text{H}] = -0.7, -0.4, 0.0$  and  $+0.2$ . The filled circles represent the co-added metal-poor and metal-rich spectra.

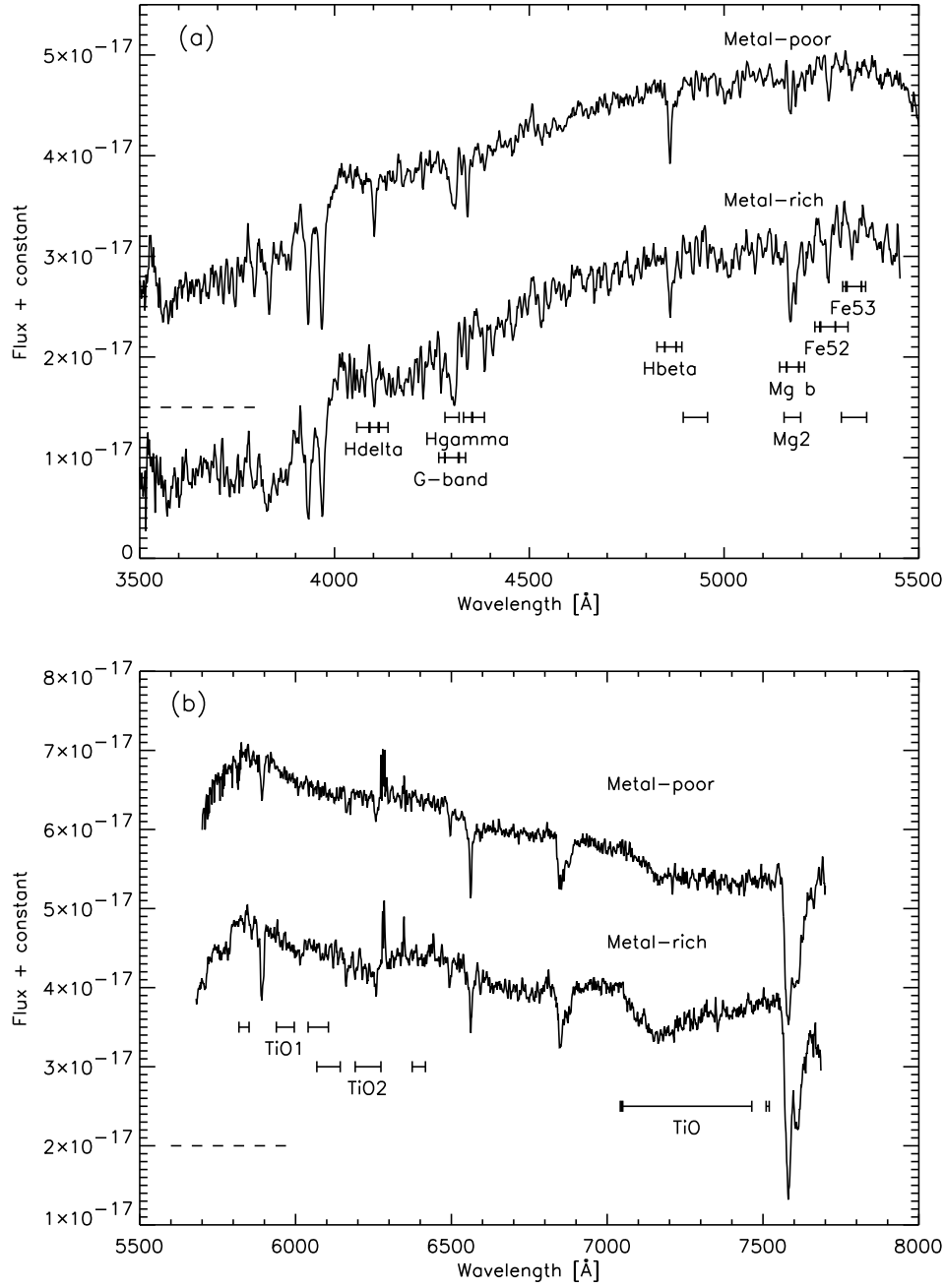


Fig. 6.— Co-added spectra of all metal-rich ( $[\text{Fe}/\text{H}] > -1.0$ ) and metal-poor ( $[\text{Fe}/\text{H}] < -1.0$ ) globular clusters. Panels (a) and (b) show the spectra from the blue and red side arms on LRIS, respectively. Lick indices used in this paper are indicated. The metal-poor spectra have been shifted upwards, as indicated by the horizontal dashed lines.

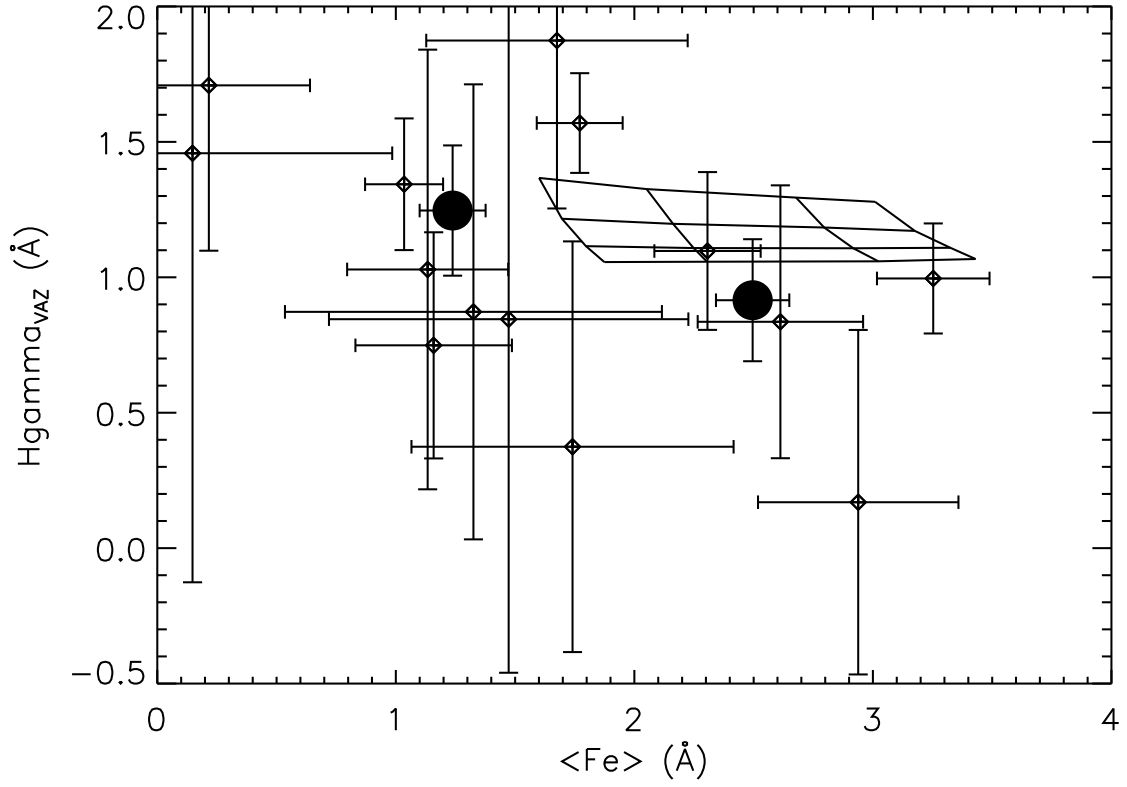


Fig. 7.— Measurements of  $\text{H}\gamma_{\text{vaz}}$  according to the Vazdekis et al. (2001) definition and  $\langle \text{Fe} \rangle$ , compared to Schiavon (2002) models.

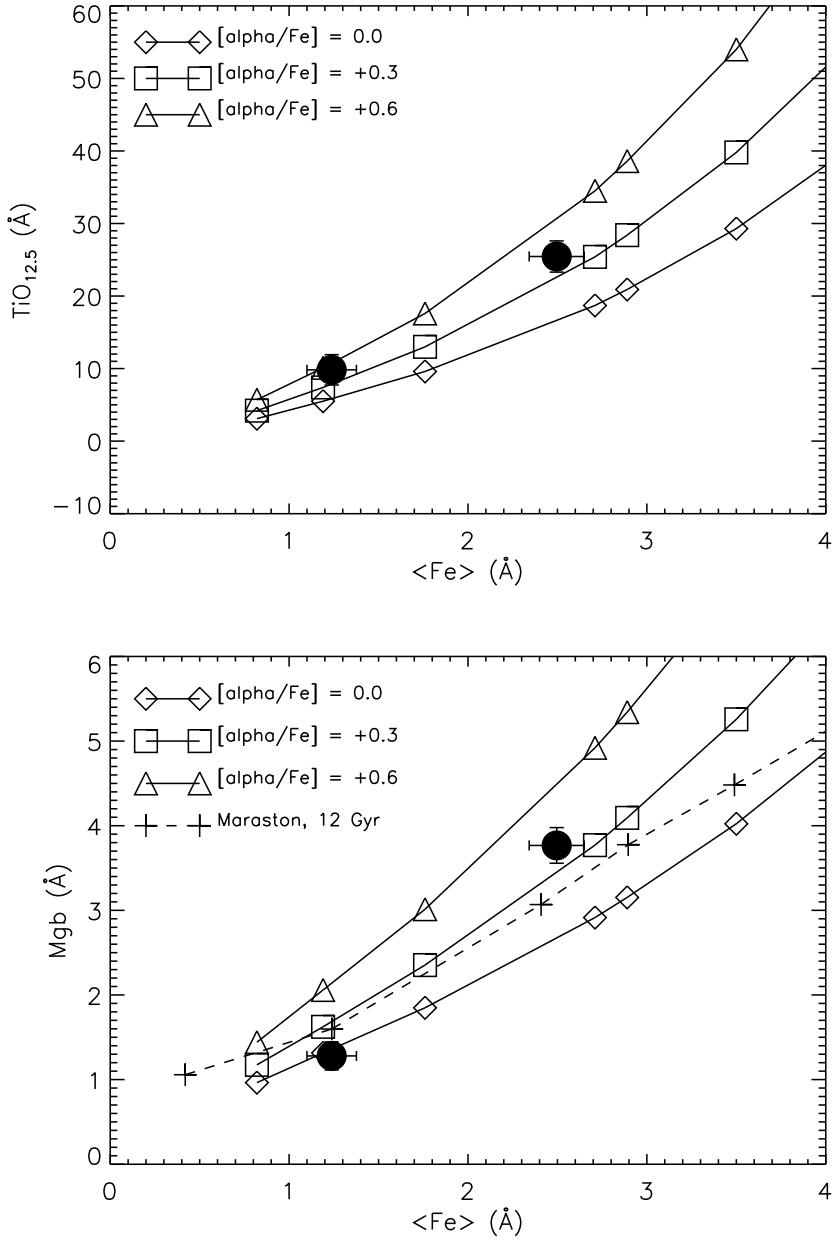


Fig. 8.—  $\text{TiO}_{12.5}$  and  $\text{Mgb}$  vs.  $\langle \text{Fe} \rangle$  for co-added metal-rich and metal-poor spectra, compared to  $\alpha$ -enhanced models by Milone, Barbuy, & Schiavon (2000). The dashed line in the  $\text{Mgb}$  vs.  $\langle \text{Fe} \rangle$  plot represents 12 Gyr Maraston models.

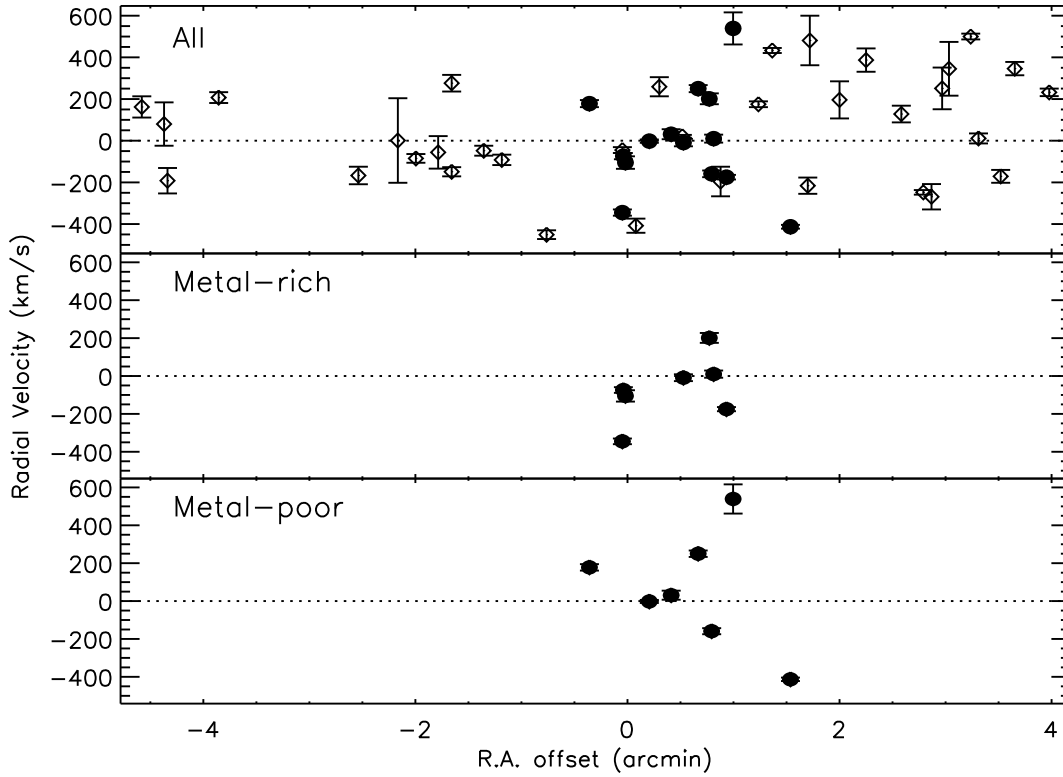


Fig. 9.— Radial velocity as a function of distance from the center along the major axis for our full GC sample combined with data from Bridges et al. (1997) (top), our metal-rich clusters only (center) and our metal-poor clusters only (bottom). Data from Bridges et al. (1997) are shown with open circles while our data are shown with filled circles. No significant evidence for rotation is seen in either sample.

Table 1. Globular cluster candidates in NGC 4594

ID	$V$	$(V-I)_0$	RV km/s	S/N		GC?
				Blue	Red	
1 / H2-06	20.28	0.92	$304 \pm 11^b$	46	-	N
2 / H2-10	20.51	1.01	$108 \pm 8$	45	55	N
4 / H2-09	20.45	0.97	$611 \pm 9$	45	44	Y
5 / H2-22	19.1 <sup>a</sup>	-	$1274 \pm 17$	19	24	Y
6 / H2-27	22.04	1.14	$227 \pm 39$	9	9	Y?
7 / C-076	21.36	0.90	$1563 \pm 77^b$	8	16	Y
8 / C-068	20.37	1.11	$849 \pm 11$	32	41	Y
9 / C-051	21.17	1.18	$1015 \pm 18$	17	25	Y
10 / C-064	21.10	0.94	$865 \pm 16$	17	23	Y
11 / C-059	21.14	1.17	$1034 \pm 19$	13	22	Y
12 / C-032	20.38	0.97	$1055 \pm 24$	25	36	Y
13 / C-042	21.19	1.26	$1225 \pm 26$	11	15	Y
15 / C-116	19.98	0.96	$1022 \pm 8$	46	46	Y
16 / C-136	21.53	1.06	$1202 \pm 17$	14	14	Y
17 / C-132	20.91	1.15	$679 \pm 15$	16	23	Y
18 / C-134	20.29	1.24	$950 \pm 15$	41	34	Y
19 / C-137	21.10	1.19	$919 \pm 30$	24	33	Y

Note. — RV = heliocentric radial velocity,  $V$  = visual magnitude. The S/N column gives the average signal-to-noise per pixel in the region 4500Å– 5000Å (blue) and 6500Å– 7000Å (red). <sup>a</sup>: This object was saturated on the WFPC2 data used in Paper I. <sup>b</sup>: Radial vel. from blue spectrum. The IDs refer to Larsen, Forbes & Brodie (2001), where coordinates are listed. The quoted errors on the radial velocities are random errors determined from the uncertainty on the cross-correlation peaks as reported by FXCOR. Additional systematic errors are  $\sim 25$  km/s (see text).

Table 2. Metallicity estimates based on the calibration in Brodie and Huchra (1990). The two bottom lines give data for the co-added metal-poor ( $[\text{Fe}/\text{H}] < -1$ ) and metal-rich ( $[\text{Fe}/\text{H}] \geq -1$ ) spectra.

Object	Individual $[\text{Fe}/\text{H}]$ estimators								$[\text{Fe}/\text{H}]$ (sp)	$[\text{Fe}/\text{H}]$ (phot)
	$\Delta$	Mg <sub>2</sub>	MgH	Gband	CNB	Fe5270	CNR	H+K		
4	$-1.59 \pm 0.37$	$-2.29 \pm 0.34$	$-2.35 \pm 0.48$	$-1.72 \pm 0.33$	$-1.96 \pm 0.34$	$-1.57 \pm 0.62$	$-1.45 \pm 0.45$	$-1.72 \pm 0.43$	$-1.86 \pm 0.14$	-1.23
5	$-1.28 \pm 0.37$	$-2.23 \pm 0.36$	$-2.06 \pm 0.52$	$-1.07 \pm 0.41$	$-1.34 \pm 0.41$	$-1.63 \pm 0.65$	$-1.30 \pm 0.49$	$-0.19 \pm 0.51$	$-1.41 \pm 0.27$	-0.42
7	$-0.87 \pm 0.39$	$-2.10 \pm 0.43$	$-1.30 \pm 0.67$	$-1.85 \pm 0.64$	$-0.78 \pm 0.97$	$-1.98 \pm 0.82$	$-2.40 \pm 0.54$	$-2.92 \pm 1.28$	$-1.80 \pm 0.31$	-1.50
8	$-0.47 \pm 0.37$	$-1.10 \pm 0.34$	$-1.17 \pm 0.49$	$-0.50 \pm 0.35$	$-0.97 \pm 0.36$	$-0.90 \pm 0.63$	$-0.96 \pm 0.46$	$-0.26 \pm 0.45$	$-0.81 \pm 0.14$	-0.67
9	$0.04 \pm 0.37$	$-0.68 \pm 0.37$	$-0.73 \pm 0.53$	$-1.80 \pm 0.43$	$0.01 \pm 0.48$	$-0.60 \pm 0.70$	$-0.63 \pm 0.48$	$0.55 \pm 0.53$	$-0.54 \pm 0.31$	-0.52
10	$-1.06 \pm 0.37$	$-2.11 \pm 0.36$	$-1.22 \pm 0.54$	$-1.33 \pm 0.40$	$-1.17 \pm 0.35$	$-1.60 \pm 0.68$	$-1.42 \pm 0.47$	$-1.44 \pm 0.48$	$-1.44 \pm 0.15$	-1.21
11	$0.24 \pm 0.37$	$-0.84 \pm 0.40$	$-1.84 \pm 0.59$	$-0.86 \pm 0.48$	$-0.63 \pm 0.59$	$-0.58 \pm 0.76$	$-0.56 \pm 0.47$	$-0.56 \pm 0.61$	$-0.74 \pm 0.23$	-0.62
12	$-0.90 \pm 0.37$	$-1.57 \pm 0.35$	$-1.24 \pm 0.51$	$-0.45 \pm 0.35$	$-1.42 \pm 0.35$	$-1.58 \pm 0.65$	$-1.24 \pm 0.46$	$-0.38 \pm 0.45$	$-1.09 \pm 0.20$	-1.23
13	$-0.59 \pm 0.38$	$-1.03 \pm 0.41$	$-1.91 \pm 0.60$	$0.16 \pm 0.68$	$-1.05 \pm 0.44$	$-1.04 \pm 0.83$	$-0.73 \pm 0.53$	$-0.59 \pm 0.66$	$-0.88 \pm 0.24$	-0.23
15	$-0.88 \pm 0.37$	$-1.62 \pm 0.34$	$-1.83 \pm 0.49$	$-1.08 \pm 0.32$	$-1.02 \pm 0.34$	$-1.17 \pm 0.62$	$-1.26 \pm 0.45$	$-0.59 \pm 0.43$	$-1.19 \pm 0.16$	-1.22
16	$-1.08 \pm 0.37$	$-1.62 \pm 0.39$	$-2.34 \pm 0.58$	$-1.09 \pm 0.46$	$-1.43 \pm 0.39$	$-1.56 \pm 0.81$	$-1.32 \pm 0.48$	$-0.84 \pm 0.53$	$-1.41 \pm 0.18$	-1.10
17	$-0.30 \pm 0.37$	$-0.32 \pm 0.38$	$-1.79 \pm 0.55$	$-0.52 \pm 0.48$	$-0.75 \pm 0.42$	$-1.02 \pm 0.71$	$0.20 \pm 0.49$	$0.36 \pm 0.53$	$-0.49 \pm 0.28$	-0.67
18	$-0.20 \pm 0.37$	$-0.08 \pm 0.35$	$-0.76 \pm 0.49$	$-0.24 \pm 0.33$	$-0.17 \pm 0.34$	$0.33 \pm 0.63$	$0.42 \pm 0.46$	$-0.15 \pm 0.43$	$-0.12 \pm 0.14$	-0.39
19	$-0.07 \pm 0.37$	$-0.78 \pm 0.36$	$-1.00 \pm 0.51$	$-0.71 \pm 0.46$	$0.24 \pm 0.37$	$-0.90 \pm 0.66$	$-0.47 \pm 0.47$	$0.11 \pm 0.47$	$-0.43 \pm 0.21$	-0.47
metal-poor	$-1.11 \pm 0.37$	$-1.82 \pm 0.34$	$-1.81 \pm 0.48$	$-1.16 \pm 0.33$	$-1.42 \pm 0.34$	$-1.44 \pm 0.61$	$-1.32 \pm 0.45$	$-0.90 \pm 0.43$	$-1.39 \pm 0.14$	-
metal-rich	$-0.24 \pm 0.37$	$-0.67 \pm 0.34$	$-1.17 \pm 0.49$	$-0.58 \pm 0.35$	$-0.54 \pm 0.35$	$-0.54 \pm 0.62$	$-0.35 \pm 0.46$	$-0.11 \pm 0.45$	$-0.54 \pm 0.13$	-

Table 3. Indices in the Lick/IDS system

Object	H $\beta$ Å	H $\gamma_A$ Å	H $\delta_A$ Å	H $\gamma_{\text{vaz}}$ Å	Fe5270 Å	Fe5335 Å	$\langle \text{Fe} \rangle$ Å	Mg <sub>2</sub> mag	Mgb Å	MgFe Å	TiO <sub>12.5</sub> Å
4	1.74 ± 0.20	1.59 ± 0.26	2.25 ± 0.29	1.34 ± 0.24	0.92 ± 0.20	1.15 ± 0.26	1.03 ± 0.16	-0.00 ± 0.00	1.01 ± 0.18	1.02 ± 0.12	2.1 ± 7.4
5	1.69 ± 0.46	0.55 ± 0.74	1.64 ± 0.83	1.03 ± 0.81	1.11 ± 0.42	1.16 ± 0.53	1.13 ± 0.34	0.01 ± 0.01	0.42 ± 0.45	0.69 ± 0.39	-24.2 ± 13.6
7	1.86 ± 1.17	3.16 ± 1.22	5.11 ± 1.60	1.46 ± 1.58	0.25 ± 0.97	0.05 ± 1.36	0.15 ± 0.84	0.03 ± 0.03	-0.25 ± 1.11	0.00 ± 0.84	-13.0 ± 15.5
8	1.61 ± 0.33	-4.07 ± 0.37	-0.39 ± 0.34	1.10 ± 0.29	1.89 ± 0.27	2.73 ± 0.35	2.31 ± 0.22	0.12 ± 0.01	2.95 ± 0.25	2.61 ± 0.17	21.9 ± 6.7
9	1.95 ± 0.53	-4.12 ± 0.67	-1.65 ± 0.86	0.17 ± 0.64	2.93 ± 0.59	2.94 ± 0.60	2.94 ± 0.42	0.17 ± 0.01	3.60 ± 0.55	3.25 ± 0.34	39.4 ± 13.8
10	3.73 ± 0.53	-0.20 ± 0.59	2.20 ± 0.69	1.71 ± 0.61	1.11 ± 0.54	-0.68 ± 0.66	0.22 ± 0.42	0.03 ± 0.01	1.20 ± 0.50	0.51 ± 0.51	10.0 ± 16.3
11	2.59 ± 0.67	-6.95 ± 0.86	-3.49 ± 0.35	0.37 ± 0.76	3.01 ± 0.77	0.48 ± 1.11	1.74 ± 0.68	0.14 ± 0.02	4.00 ± 0.58	2.64 ± 0.55	16.7 ± 15.1
12	2.85 ± 0.38	-3.04 ± 0.40	1.66 ± 0.42	0.75 ± 0.42	0.75 ± 0.39	1.57 ± 0.52	1.16 ± 0.33	0.08 ± 0.01	1.24 ± 0.51	1.20 ± 0.30	8.6 ± 7.8
13	2.91 ± 0.82	-3.85 ± 1.27	1.65 ± 1.46	0.85 ± 1.31	1.05 ± 0.97	1.90 ± 1.16	1.47 ± 0.75	0.14 ± 0.02	2.69 ± 0.90	1.99 ± 0.61	30.0 ± 24.6
15	2.10 ± 0.22	-0.54 ± 0.21	2.35 ± 0.21	1.57 ± 0.18	1.70 ± 0.21	1.84 ± 0.30	1.77 ± 0.18	0.06 ± 0.01	1.52 ± 0.22	1.64 ± 0.15	28.3 ± 7.0
16	3.31 ± 0.65	-1.33 ± 0.90	2.83 ± 0.86	0.87 ± 0.84	0.90 ± 0.96	1.75 ± 1.25	1.33 ± 0.79	0.05 ± 0.02	2.11 ± 0.67	1.67 ± 0.57	-6.4 ± 24.1
17	1.61 ± 0.58	-5.00 ± 0.66	-3.44 ± 0.94	1.87 ± 0.62	2.48 ± 0.67	0.87 ± 0.87	1.68 ± 0.55	0.20 ± 0.02	3.77 ± 0.66	2.51 ± 0.47	34.7 ± 9.7
18	1.41 ± 0.26	-6.76 ± 0.26	-4.81 ± 0.25	1.00 ± 0.20	3.80 ± 0.26	2.70 ± 0.39	3.25 ± 0.24	0.21 ± 0.01	4.40 ± 0.26	3.78 ± 0.18	10.9 ± 8.2
19	1.67 ± 0.38	-5.36 ± 0.61	-1.77 ± 0.77	0.84 ± 0.50	2.30 ± 0.44	2.93 ± 0.53	2.61 ± 0.35	0.15 ± 0.01	4.32 ± 0.40	3.36 ± 0.27	32.6 ± 10.4
metal-poor	2.39 ± 0.17	-0.45 ± 0.23	2.19 ± 0.28	1.25 ± 0.24	1.15 ± 0.14	1.32 ± 0.24	1.24 ± 0.14	0.05 ± 0.00	1.28 ± 0.17	1.26 ± 0.11	9.8 ± 2.1
metal-rich	1.78 ± 0.17	-5.26 ± 0.30	-2.01 ± 0.35	0.92 ± 0.23	2.73 ± 0.22	2.26 ± 0.21	2.50 ± 0.15	0.16 ± 0.01	3.77 ± 0.21	3.07 ± 0.13	25.5 ± 2.2